Atmospheric Research 325 (2025) 108159



Contents lists available at ScienceDirect

Atmospheric Research

journal homepage: www.elsevier.com/locate/atmosres





Observational study of a quasi-stationary mesoscale convective system during extreme rainfall on 8 August 2022 in Korea

Hee-Ae Kim [a], Chang-Hoi Ho [a,b,*], Jinwon Kim [b], Eun-Kyoung Seo [c], Seon Ki Park [b]

[a] School of Earth and Environmental Sciences, Seoul National University, Seoul, Republic of Korea
[b] Department of Climate and Energy Systems Engineering, Ewha Womans University, Seoul, Republic of Korea
[c] Department of Earth Science Education, Kongju National University, Kongju, Republic of Korea

ARTICLE INFO

Keywords:
Seoul flood
Quasi-stationary mesoscale convective system
Extreme weather
Radar
Mesoscale surface front
Cloud hydrometeor

ABSTRACT

On 8 August 2022, a quasi-stationary mesoscale convective system (MCS) produced prolonged extreme rainfall ($>$ 100 mm h^{-1}) over the Seoul metropolitan area, Republic of Korea. These organized convective systems, primarily composed of convective components with interspersed stratiform elements, are characterized by the successive local generations of convective cells. This study analyzes data from multiple observational platforms to understand the formation of the MCS and its microphysical evolution. The convective cells were initiated just off the west coast near Seoul, along the boundary between warm and cold air masses. Low-level convergence and favorable environmental conditions, including low lifting condensation level, level of free convection, and large convective available potential energy, facilitated the triggering of these cells. As the cells moved inland, they intensified rapidly due to the land-sea surface-friction contrast. Radar data show that as the MCS matured, reflectivity increased and the differential reflectivity decreased downward above the melting level, indicating the growth of ice crystals and graupels. The evolution of microphysical structure led to increases in both the mean diameter (D_m) and the number concentration (N_T) of raindrops. This observation also suggests that the rainfall intensity was more closely related to the increase in N_T than D_m during the period of heavy downpours. This study improves our understanding of the mesoscale processes related to extreme rainfall in Korea, critical for forecasting local heavy rainfall.

1. Introduction

Heavy summer rainfall plays a critical role in the occurrence of hydrological natural disasters in the Republic of Korea (hereafter Korea). According to the Ministry of the Interior and Safety (2024), torrential rainfall is responsible for more than 60% of damage caused by all natural disasters in Korea over the most recent decade (2013–2022). Since much of the damage by extreme rainfall occurs in association with mesoscale convective systems (MCSs) (Lee and Kim, 2007; Jeong et al., 2016), understanding the mechanisms behind the development and organization of convections into an MCS is critical for improving heavy rainfall forecasting. MCSs occur in various forms. Among these, quasi-stationary (and/or back-building) systems, a linear MCS characterized by convective cells aligned in the direction of the MCS movement (Parker and Johnson, 2000; Schumacher and Johnson, 2005), often concentrate heavy rainfall in small areas to cause large damages.

The development of MCSs is influenced by both synoptic environments and mesoscale processes. In particular, quasi-stationary MCSs depend on mesoscale phenomena such as the cold pool, orographic lifting, and mesoscale convective vortices (e.g., Corfidi, 2003; Schumacher and Johnson, 2005; Johnson and Hamilton, 1988; Xu et al., 2012; Jeong et al., 2016; Park and Park, 2020). Schumacher and Johnson (2005) showed that nearly half (47%) of the quasi-stationary weather systems in the central United States were induced and maintained by outflows generated by evaporative cooling of raindrops in convective downdrafts. If heavy clouds limit daytime surface solar heating and the near-surface air is close to saturation, the generation of a strong cold pool becomes difficult (Schumacher, 2017). In such circumstances, alternative mechanisms such as mesoscale convective vortices and orographic lifting become important for providing the momentum necessary for MCS initiation (Rasmussen et al., 2014, 2016). In Korea, which is characterized by highly humid summer environments

* Corresponding author at: Department of Climate and Energy Systems Engineering, Ewha Womans University, 52, Ewhayeodae-gil, Seodaemun-gu, Seoul 03760, Republic of Korea.
E-mail address: hoch@ewha.ac.kr (C.-H. Ho).

https://doi.org/10.1016/j.atmosres.2025.108159
Received 9 December 2024; Received in revised form 2 April 2025; Accepted 14 April 2025
Available online 15 April 2025
0169-8095/© 2025 The Authors. Published by Elsevier B.V. This is an open access article under the CC BY-NC license (http://creativecommons.org/licenses/by-nc/4.0/).

and complex terrain, the combination of weak cold pools and orographic lifting has been known to be effective in triggering heavy rainfall events (Park and Park, 2020).

Accurate prediction of MCS formation and evolution remains challenging despite advances in numerical modeling (Wandishin et al., 2008, 2010) mainly due to the lack of representing the physical processes involved in rainfall such as convections (Schumacher and Johnson, 2005) and cloud microphysics, as well as the sensitivity to environmental conditions such as low-level moisture distribution (Peters et al., 2017). The general characteristics and structures of MCSs have been extensively documented in pioneering studies (Maddox, 1980; Zipser, 1977; Houze Jr. et al., 1990; Biggerstaff and Houze Jr., 1991; Biggerstaff and Houze Jr., 1993). While some MCS research, particularly those for detailed storm-scale dynamics, benefits from high-resolution numerical modeling, observational analyses are crucial for understanding the environmental conditions and evolution of these systems. Many MCSs studies are based on observations from conventional networks including surface weather systems, rawinsonde, wind profilers, and radar (Bluestein and Jain, 1985; Houze Jr. et al., 1989; Kim and Lee, 2006; Jirak and Cotton, 2007; Wu and Luo, 2016) as well as special field campaigns (Johnson and Hamilton, 1988; Cifelli et al., 2002; Davis et al., 2004; Wang et al., 2014) for detailed analyses of MCS evolution. Advent of the dual-polarimetric radar and satellite observations has significantly improved to our understanding of the dynamics and microphysics of convective cells (Rowe and Houze Jr., 2014; Hu et al., 2020; Li et al., 2020; Feng et al., 2021). Multi-platform observational studies can provide valuable insights into the formation mechanisms and maintenance of MCSs, especially rainfall events.

On 8 August 2022, the Seoul metropolitan area in Korea experienced extreme rainfall due to a quasi-stationary MCS characterized by successive developments of convective cells that were subsequently organized in a narrow band over the region. However, this event occurred without typical environmental features known to support continuous local development of convective cells, such as strong cold pools or orographic lifting. This unique case provides an opportunity to investigate less-understood mechanisms of MCS formation and maintenance. By analyzing observational data from multiple platforms including operational weather data, surface observations in a dense network, and upper-air measurements, this study documents the formation mechanism of these convective cells and their microphysical evolutions from the initial development to the maturity. This analysis aims to enhance our understanding of the meteorological factors that drive extreme local rainfall in Korea, with particular focus on the environmental conditions that supported the persistence of this unique system.

In the following sections, we describe the methodology and observational datasets used in this study. Presentation of detailed analyses of the convection triggering mechanisms and microphysical processes during the heavy rainfall event follows, with particular attention to the environmental conditions that supported the quasi-stationarity of the system. We conclude and discuss the implications of our findings for improving our understanding of extreme rainfall events in similar synoptic and mesoscale environments.

2. Data and methods

This study analyzes the environmental factors and cloud microphysical characteristics associated with a heavy rainfall MCS event that occurred over Korea on 8 August 2022. The three-dimensional structure and evolution of the MCS are analyzed using various observational platforms including: surface meteorological data from automated weather stations (AWSs) and ocean buoys, upper-air soundings, weather radar and satellites. Microphysical characteristics and their temporal evolutions are investigated using operational weather radar and surface disdrometer observations. The analysis is conducted for two spatial domains: a larger domain covering a northeastern Asia region around the Korean Peninsula (Fig. 1a), and a smaller domain focused on the Seoul metropolitan area (Fig. 1b) where the extreme rainfall occurred.

2.1. Surface observations

We used a comprehensive data set of surface meteorological observations. The primary data source is AWS data from Korea Meteorological Administration (KMA), which provides temperature, wind, and rainfall data, particularly useful for analyzing rainfall and surface wind distribution. Since AWS observations are limited to land areas, additional wind data are obtained from ocean buoys operated by KMA, and ocean research stations (ORS) and tide stations employed by Korea Hydrographic and Oceanographic Agency (KHOA). All these data sources provide observations at 1-min intervals. The KMA AWS and KHOA ocean buoy data undergo quality control procedures conducted by the agencies as part of their operational processes, thus no additional quality control is necessary in this study. Note that KMA AWS stations operate without on-site personnel, so that these data are not used for official weather summaries or climate statistics.

2.2. Sounding (upper-air) data

To examine vertical atmospheric structure, rawinsonde are obtained from two upper-air stations: Baekryeongdo and Osan, located 100 km to the northwest and 35 km to the south of the rainfall area, respectively (red squares in Fig. 1b). At these stations, rawinsondes are launched every six hours (3, 9, 15, and 21 LT) to observe the vertical profiles of

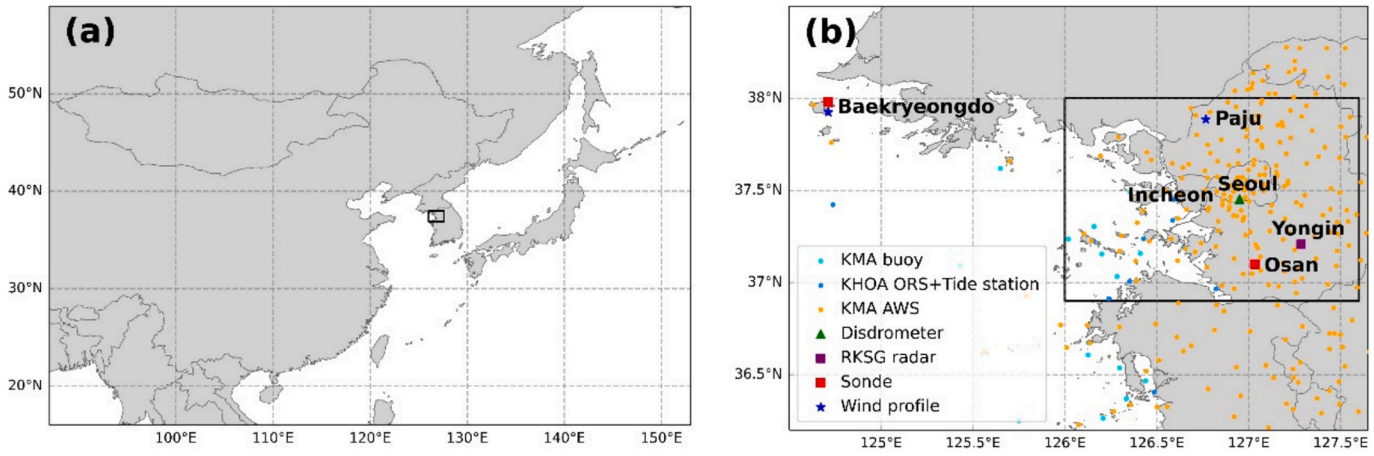


Fig. 1. The study area: **(a)** the East Asian domain for analyzing the synoptic-scale environment and **(b)** the heavy rainfall area (inner box). Fig. 1b presents the types and locations of the observation sites around the heavy rainfall area.

temperature, humidity, wind, and other atmospheric variables. The sounding data are used to calculate atmospheric instability indices. To compensate for the coarse temporal resolution and to obtain detailed wind information, wind profiler data with 10-min resolution from Baekryeongdo and Paju are also used (blue stars in Fig. 1b). These wind profilers transmit ultrahigh frequency (300–3000 MHz) radio waves upward and analyze the return signals to retrieve vertical wind profiles. In particular, in this study we use the low-mode wind profiler data, which cover up to 5 km above ground level (AGL) with vertical resolutions of about 50 m, to analyze low tropospheric winds.

2.3. Remote sensing data

Weather radar and satellite data are used to complement surface and upper-air data in analyzing hydrometeor characteristics within the MCS regions, as well as the ambient wind field associated with the MCS. Radar data are obtained from the National Oceanic and Atmospheric Administration (NOAA)-operated RKSG Weather Surveillance Radar-1988 Doppler, a 2.94-GHz S-band dual-polarimetric radar with 0.925° beam widths and 250-m range resolution. As they can transmit and receive electromagnetic waves in both the horizontal and vertical planes, dual-polarimetric radars can provide detailed information on the precipitating and cloud particles including the size, shape, and orientation through the dual-polarimetric variables such as reflectivity (Z_H) and differential reflectivity (Z_{DR}). To improve the accuracy of radar data and enhance data interpretation, quality control and coordinate transformation are performed using the methodology of Kim et al. (2024). To analyze the characteristics of cloud and precipitating particles within convective areas, regions within the rainfall area are identified following Steiner et al. (1995). Within these convective regions, the frequency of Z_H and Z_{DR} at each bin is calculated and subsequently normalized by the maximum frequency in the entire dataset. The normalization is applied to the contoured frequency by altitude diagrams (CFADs) analysis, which provides a statistical representation of storm properties in the vertical (Yuter and Houze Jr., 1995).

In addition to the rainfall distribution and hydrometeor characteristics, we analyze the type and distribution of precipitating and cloud particles detected by radar using the hydrometeor classification algorithm (HCA) of Park et al. (2009) and Mahale et al. (2014). The classification scheme relies on five principal variables: Z_H, Z_{DR}, correlation coefficient (ρ_{hv}), and texture parameters of both Z_H and differential phase (Φ_{DP}). By aggregating these variables using the trapezoidal weighting function, the HCA categorized radar echoes into ten hydrometeor classes: ground clutter and anomalous propagation (GC/AP), biological scatter (BS), dry snow (DS), wet snow (WS), ice crystals (CR), graupel (GR), large drops (BD), light and moderate rain (RA), heavy rain (HR), and mixture of rain and hail (RH). Since radar resolution volumes frequently contain mixtures of hydrometeors, the algorithm identifies the most dominant class in each volume. Although incorporating specific differential phase (K_{DP}) can improve the estimation, the RKSG radar data used in this study provide K_{DP} only for a limited range of elevation angles. Thus, dedicated K_{DP} retrieval algorithm is required before K_{DP} is incorporated into the analysis. This is beyond the scope of this study, and K_{DP} is excluded from the analysis in this study.

Raindrop distributions are analyzed using the drop size distribution (DSD) algorithm of Ho et al. (2023) and Brandes et al. (2004a, 2004b) due to their simple yet intuitive approach, with minor modifications to the original coefficients. The algorithm employs empirical relationships between radar-derived variables to estimate DSD parameters (Brandes et al., 2004a; Ho et al., 2023). This scheme provides polarimetric radar-based DSD parameters including the mass-weighted average diameter (D_m, μm), liquid water content (W, g m^{-3}), and total number concentration (N_T, m^{-3}) using the power-law forms in Eqs. (1)–(4):

$$D_m = 0.08 Z_H^{0.037} Z_{DR}^{1.2} \quad (1)$$

$$N_t = \log_{10}\left(\frac{W}{6.73 \times 10^{-5.0} D_0^4}\right) \quad (2)$$

$$W = 0.00083 Z_H^{0.09} Z_{DR}^{-3.0} \quad (3)$$

$$D_0 = 0.171 {Z_{DR}}^3 - 0.725 {Z_{DR}}^2 + 1.479 Z_{DR} + 0.717 \quad (4)$$

Comparison of the calculated DSD values against the Parsivel^2 disdrometer measurements at the Gwanak Mountain station in Seoul (Lee et al., 2023) demonstrates that retrievals based on the Ho et al. (2023) scheme produce reasonable value ranges and patterns of variation (not shown).

To understand the development of convective cells and the dry-air flow around them, we used the KMA Geo-KOMPSAT-2A (GK-2A) / Advanced Meteorological Imager (AMI) data. GK-2A has 16 channels ranging from the visible to the thermal infrared including three water vapor bands of central wavelengths of 6.3, 6.9, and 7.3 μm that detect moisture in different atmospheric layers (Kim et al., 2021). In this study, the brightness temperature from the 6.9-μm band is used to analyze the water vapor flow in the mid-troposphere near 500 hPa. This band provides measurements over East Asia at 2-km resolution with 10-min temporal intervals.

3. Description of the Seoul flooding event

On 8 August 2022, Seoul experienced extreme rainfall with a record-breaking rainfall intensity of 141.5 mm h^{-1}, which caused severe urban flooding and significant damage. To understand the meteorological conditions that led to this extreme event, this section presents the synoptic pattern and evolution of the rainfall distribution. The synoptic weather maps at four levels (surface, 850 hPa, 500 hPa, and 200 hPa) at 9:00 local time (LT) on 8 August illustrates the complex interaction between different air masses (Fig. 2).

The surface weather map shows a sharp contrast in wind directions across the northern boundary of Korea (Fig. 2a) as southwesterly winds dominate over Korea while northerly winds prevail near the border between North Korea and Manchuria. This wind pattern is accompanied by extensive cloud cover (overcast) across Korea. Wind directions are aligned with the 850 hPa synoptic-scale pressure patterns (Fig. 2b). At this level, a well-defined low-level convergence zone develops over Korea due to the interaction of two distinct air masses. A high-pressure system over northern inland China and a low-pressure system north of Manchuria generate northerly winds that bring cold and dry air towards Korea, while southerly winds along the periphery of the Western North Pacific subtropical high advect warm and moist air into the region. The convergence of these contrasting airflows results in the formation of a frontal boundary and strong low-level convergence over the southern half of Korea.

At 500 hPa (Fig. 2c), the pressure pattern reflects the development of a low-pressure system centered on Manchuria, extending into the mid-troposphere. A weak trough extends southward from this system, passing over Korea, contributing to enhancement of atmospheric instability. At the upper level (200 hPa, Fig. 2d), a well-defined jet stream (marked by a red thick line) extends from Mongolia to the north of Korea. As it decelerates over Manchuria, upper-level convergence occurs the southern jet stream exit region (north of the Korea-Manchuria border), leading to subsidence which enhances cold air advection into Korea from Manchuria. The interaction of the cold northerly flow with the warm and moist southerly flow south of Seoul establishes a temperature boundary, which likely triggered intense convection and torrential rainfall over Korea. In addition, a weak high-pressure system over inland China influences the upper atmosphere over Korea. Although the ridge and trough patterns are not particularly pronounced, this system contributes to wind divergence in the mid-to-upper levels over central Korea. The combination of the jet stream position, enhanced surface

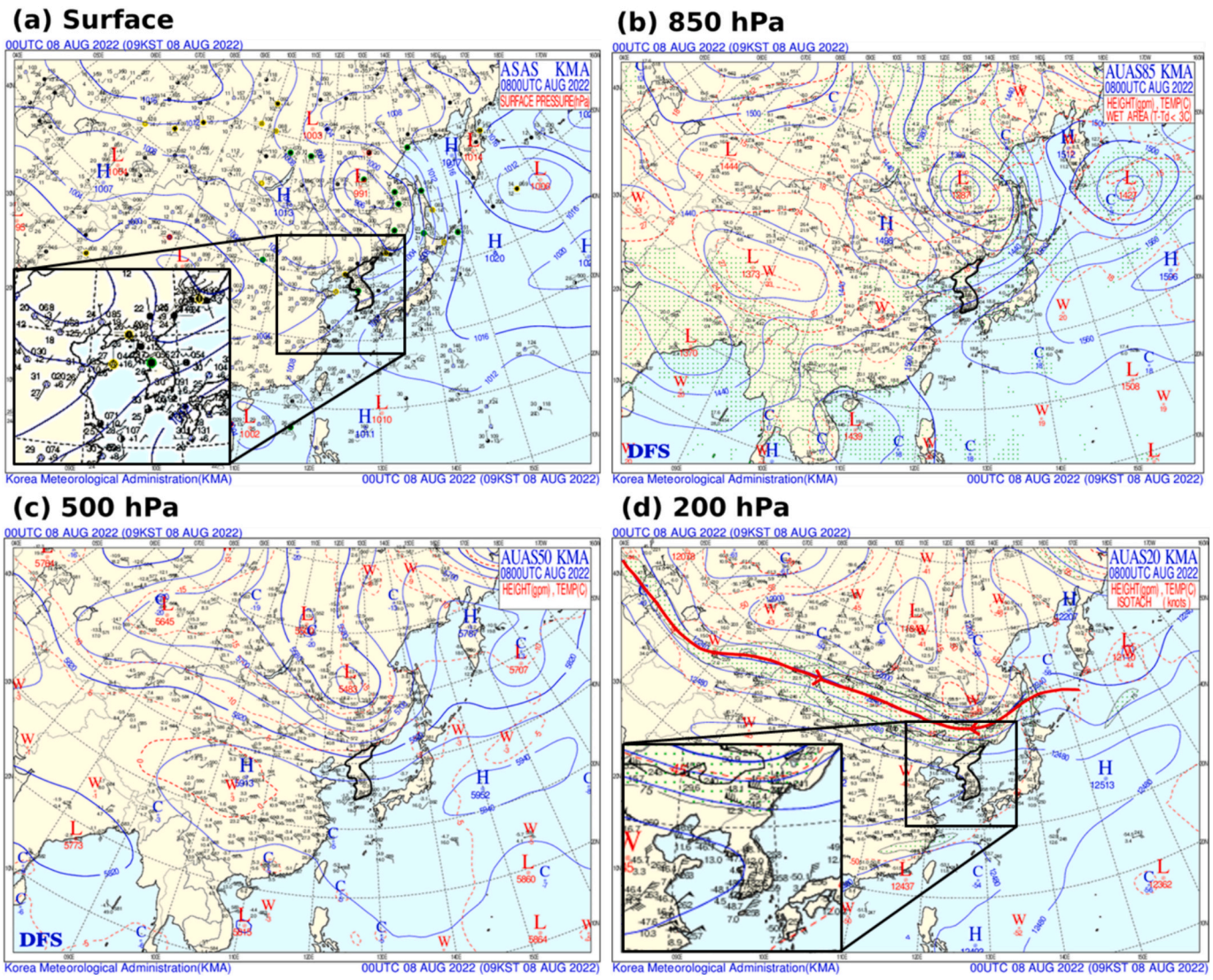


Fig. 2. Synoptic weather maps at (a) the surface, (b) 850 hPa, (c) 500 hPa, and (d) 200 hPa at 9:00 LT on 8 August 2022. The boundary of the Korean Peninsula is outlined in black. In panels (a) and (c), an extended map highlights Korea and the surrounding region. in panel (d), the thick red line represents the upper-level jet, while the red angular line indicates the entrance (>) and exit (<) regions of the jet streak. (For interpretation of the references to colour in this figure legend, the reader is referred to the web version of this article.)

temperature contrasts, and upper-level divergence creates a favorable environment for developing severe weather.

About 10 h after the synoptic conditions shown in Fig. 2, the radar reflectivity indicates rapid intensification and organization of the MCS over Seoul (Fig. 3). Around 18:52 LT, the first cell *A* forms near the west coast of Incheon and moves inland towards the east, intensifying rapidly (Fig. 3a). Two additional cells, *B* and *C*, develop consecutively in the same location about 30 min apart (Fig. 3b and c). The trailing cell moves faster than the leading cell and eventually merges with it, to form a single, organized linear convective system (Fig. 3d). Unlike typical squall lines, where the mid-to-upper-level winds are angled relative to the convective line allowing hydrometeors to be advected backwards to form a stratiform rainfall region, this case exhibits a solid linear structure with small stratiform rainfall. This is mainly because the mid-level winds are parallel to the convective line (east-west direction) and transport hydrometeors eastward along the line to generate minimal stratiform clouds. The merged system then continues propagating eastwards along the pre-existing linear track, intensifying further, to reach the maximum rain rate at 20:47 LT (Fig. 3e). In the later stage, the MCS evolves from an initially cellular structure into a larger, more organized linear system resembling a frontal structure (Fig. 3f). This study focuses on the stages from Figs. 3a to 3e where the quasi-stationary nature of the MCS is most evident. Fig. 3b, c, and e are referred to as S1, S2, and S3 hereafter.

4. Formation and microphysical evolution of the MCS

4.1. Formation environment

This section examines the environment that lead to successive generations of convective cells in a small upstream area during the MCS formation by analyzing the upper-air and surface data around the heavy rainfall area. The upper-air soundings from Osan and Baekryeongdo are presented in skew T-log p diagrams in Fig. 4, as the heavy rainfall event was occurring between these two stations. To track the evolution of the large-scale environment during the event, observations at successive time slices are investigated. Data from the periods before (blue) and after (red) the initiation of the first convection cell are selected to analyze the vertical structure of the atmosphere, with emphasis on the period closest to the rainfall event. Specifically, soundings at Osan (9:00 LT and 21:00 LT) and Baekryeongdo (15:00 LT and 21:00 LT) are analyzed, focusing on the rainfall between 18 LT and 21 LT.

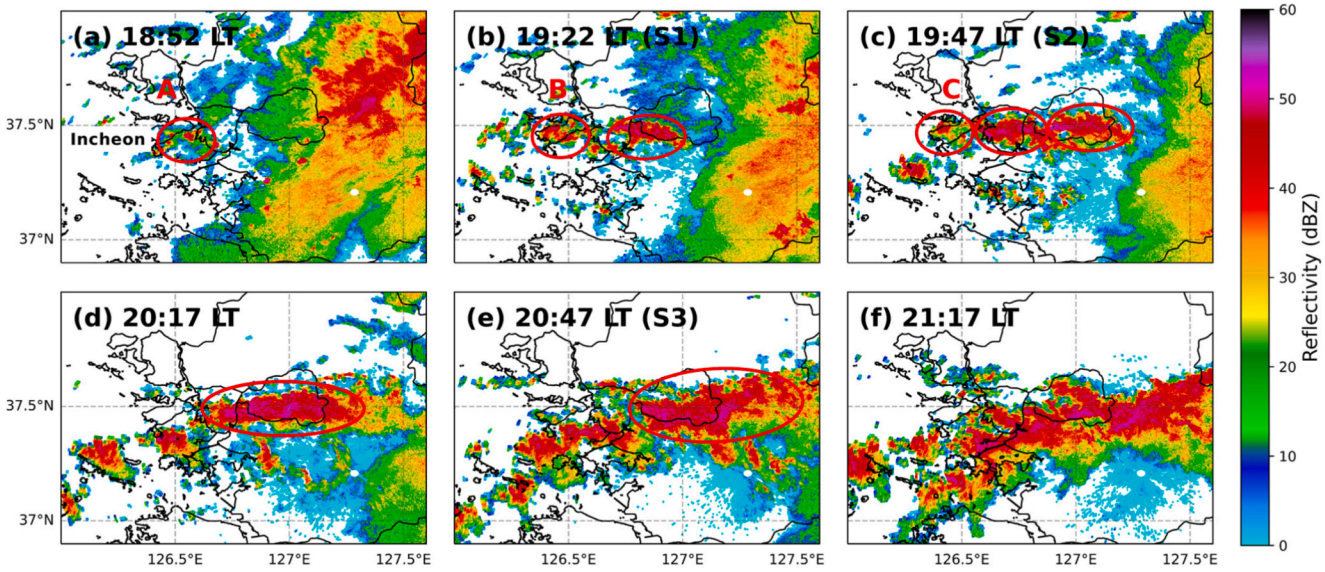


Fig. 3. Reflectivity factor (shading) at horizontal polarization from the RKSG radar at a 1.3° elevation angle, presented at intervals of 25–30 min between 18:52 and 21:17 LT on 8 August 2022: (a) 18:52, (b) 19:22, (c) 19:47, (d) 20:17, (e) 20:47, and (f) 21:17 LT. Three distinct convective cells (A, B, and C) and their evolution are marked with red circles. (For interpretation of the references to colour in this figure legend, the reader is referred to the web version of this article.)

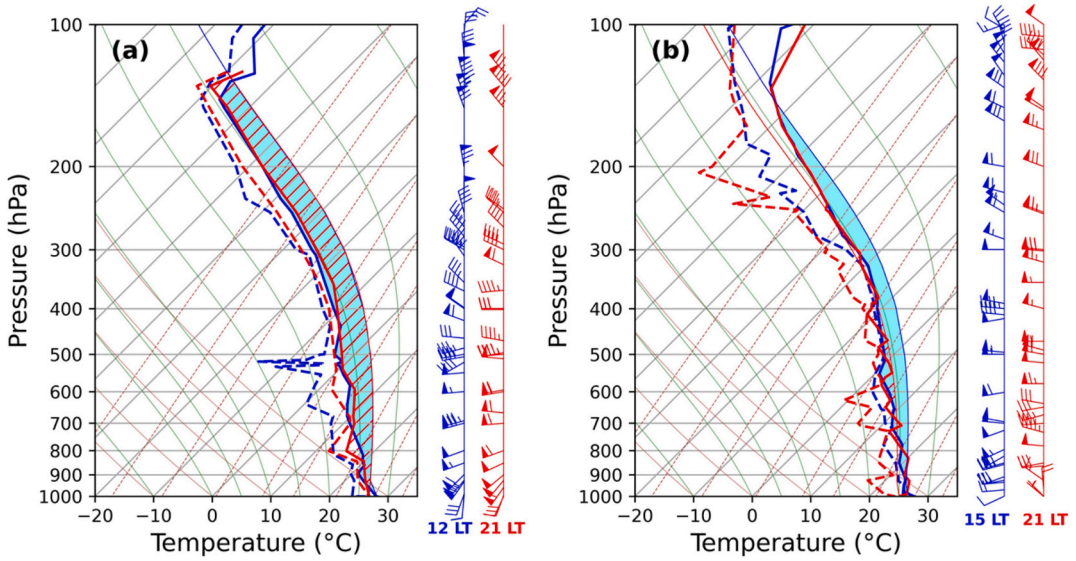


Fig. 4. The skew *T*-log *p* chart from rawinsonde data on 8 August 2022: (a) Osan at 9:00 LT (blue) and 21:00 LT (red), (b) Baekryeongdo at 15:00 LT (blue) and 21:00 LT (red). The solid and dashed lines represent the vertical profiles of temperature and dew point, respectively. The red hatched area and the cyan shaded area indicate the convective available potential energy. The wind barbs on the right show the wind profiles for each observation time. (For interpretation of the references to colour in this figure legend, the reader is referred to the web version of this article.)

At Osan at 09:00 LT, a dry air intrusion is clearly shown in 500–600 hPa layer prior to the MCS development layers (Figs. 4a). This is consistent with low equivalent potential temperature advection towards the Korean Peninsula through Manchuria as seen in the upper-level weather map at the same time (not shown here). By 21:00 LT, compared to the earlier soundings, the Osan station shows close alignments between the air temperature and dew point temperature profiles, indicating moisture recharging throughout the deeper layer, particularly below 800 hPa. At Baekryeongdo, they are farther apart, indicating drier conditions through all layers (Fig. 4a and b). The moist conditions developing south of the heavy rainfall area may be critical for both the initiation and sustained development of this MCS case.

The wind barbs on the right sides of Fig. 4a and b infer dynamic conditions of ambient atmosphere near the rain band. Both profiles show strong wind shear in the low level, but their wind patterns differ notably despite the proximity of these stations (~200 km). At Osan, located ~50 km to the south of the rainfall area (Fig. 4a), winds veer from southwesterly to westerly below 700 hPa, indicating warm air advection in the layer (Holton, 2004). In contrast, at Baekryeongdo, located to the north of the rainfall area (Fig. 4b), the wind direction shifts notably before and after rainfall onset. Before the rainfall, westerly winds dominate in the lower level. Just prior to rainfall initiation, the winds back from northwesterly to westerly, indicating cold air advection from the north of the rainfall area (Holton, 2004). This interaction between the cold air advected from the north and the persistent warm southerly flow triggered the formation of rainfall.

Thermodynamic parameters computed using the soundings are provided in Table 1. The total precipitable water (TPW) exceeds 60 mm

Table 1
Severe weather parameters at the Osan and Baekryeongdo stations on 8 August 2022.

Station	Parameters	3:00 LT	9:00 LT	15:00 LT	21:00 LT
Osan	TPW (mm)	69.7	64.4	–	72.9
	LCL (m)	306	323	–	119
	LFC (m)	470	435	–	119
	CAPE (J kg^{-1})	20	2372	–	1955
	EL(m)	1295	14,389	–	14,534
	θ_{e-850} (K)	348	349	–	353
Baekryeongdo	TPW (mm)	69.1	71.8	74.8	64.6
	LCL (m)	349	272	349	263
	LFC (m)	418	2069	349	2255
	CAPE (J kg^{-1})	0	224	1213	13
	EL (m)	444	8014	13,536	2832
	θ_{e-850} (K)	351	348	351	345

for both soundings all day on 8 August 2022. According to the practical guide to forecasting techniques in KMA (Korea Meorological Administration (KMA), 2023), TPW values above 25 mm at both stations indicate a high probability for thunderstorm developments in Korea. At Osan, both the lifting condensation level (LCL) and level of free convection (LFC) remain low, around 300 m and 400 m AGL, respectively. They stay close until 15:00 LT, then, they rapidly drop to 119 m at 21:00 and merge with each other. The LCL, which represents the height where an air parcel becomes saturated while lifted adiabatically, strongly correlates with the cloud base height (Craven et al., 2002). A low LCL suggests that cloud formation can be initiated with a small forcing (Wilde et al., 1985; Yin et al., 2015). Similarly, the LFC, the level where a rising air parcel becomes more buoyant than its environment after reaching the LCL so that it can continue to rise freely, is also low. These low LCL and LFC provide favorable conditions for sustained cloud developments. In contrast, at the Baekryeongdo station, the LCL remains low (~300 m), but the LFC increases significantly to 2 km after 15:00 LT.

Once above the LFC, clouds rise to their equilibrium level (EL). The buoyant energy that drives this ascent from the LFC to the EL is reflected in convective available potential energy (CAPE), which, by definition, increases as the LFC decreases and the EL increases. The CAPE area at each station is presented for before (shaded in cyan) and after (red-hatched area) the observational times in Fig. 4. At Osan, the LFC decreases while the EL increases, creating conditions favorable for larger CAPE values. In moist environments over Korea, a CAPE value exceeding ~1000 J kg^{-1} indicates a high potential for convection development (Korea Meorological Administration (KMA), 2023). Prior to the MCS formation, CAPE values are recorded at 2372 J kg^{-1} around 09:00 LT at Osan and 1213 J kg^{-1} around 15:00 LT at Baekryeongdo. Due to missing observations at 15:00 LT at Osan and the increasing trend of CAPE at the Baekryeongdo, the CAPE value at Osan may exceed 2372 J kg^{-1}, considering daytime heating effects. Overall, the CAPE distribution suggests that the atmosphere around the rainfall area is highly unstable, particularly to the south of the rainfall region.

Moreover, along with changes in low-level wind direction (Fig. 4), the interaction of different air masses is also evident in the equivalent potential temperature variations at the 850 hPa level ($\theta_{e\text{-}850}$). At Osan, $\theta_{e\text{-}850}$ increases from 349 K to 353 K while at Baekryeongdo, it decreases from 348 K to 345 K. Compared to the early morning hours, this interaction between southerly wind and northerly winds intensifies during the daytime, producing strong contrasts in temperature and humidity and resulting in the formation of a surface front between the Osan and Baekryeongdo stations.

The influence of wind changes on the formation and development of the MCS is further analyzed using the high-resolution wind profiler data. For better clarity in Fig. 5, the raw data, originally recorded at 10-min intervals with a 50-m vertical resolution, are resampled to 20-min intervals and 100-m vertical resolution for the Baekryeongdo and Paju stations, which are located ~100 km to the northwest and ~ 20 km to the north of the rain bands, respectively.

The winds over Baekryeongdo show that westerly winds prevail until around 15:00 LT (Fig. 5a), then turn into northwesterlies (backing) by 16:30 LT, about two hours before the first convective cell is formed. The wind backing, highlighted by the blue box in Fig. 5a, continues as the MCS develops into its mature stage. This feature is consistent with the backing Fig. 4b. In contrast, the wind profiler data from Paju show that westerly winds prevail at low levels throughout the period (Fig. 5b), except for the near-surface layer below 500 m AGL. The persistent westerly winds extending through a considerable depth of the lower atmosphere continue after the formation of the MCS and may act as a barrier against southerly warm-air advection, resulting in the west-east alignment of the convective cells over the rainfall area. The barrier-like boundary extends in west-to-east orientation, parallel to the direction of cell development.

The wind convergence observed in the radiosonde and wind profiler data, comprising northwesterly winds to the north and southwesterly

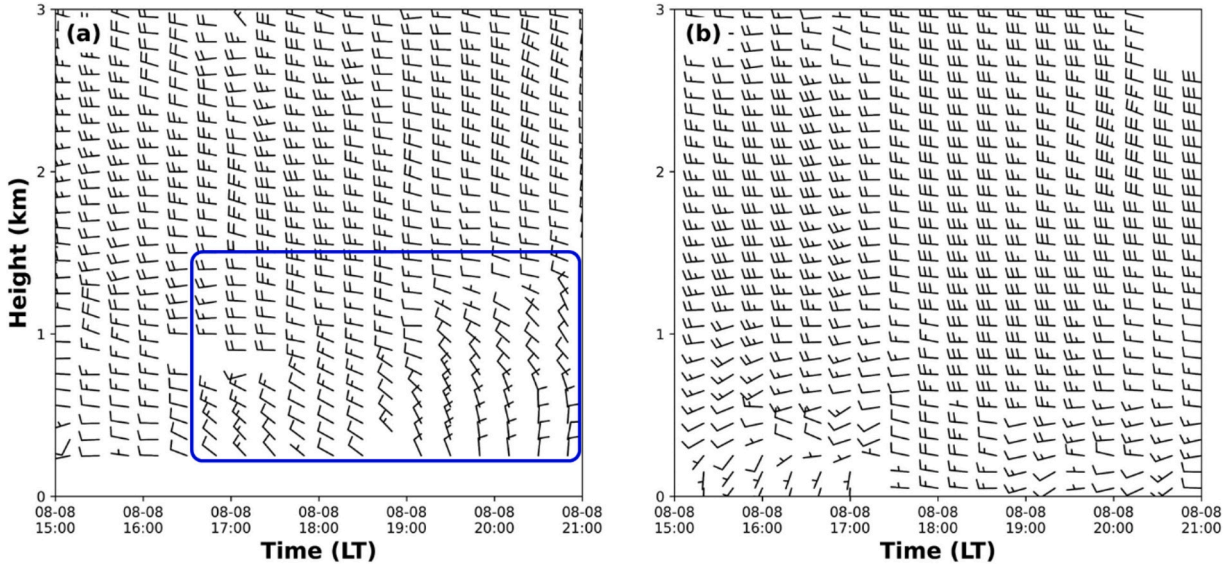


Fig. 5. Time-height wind profiles from the wind profiler at (a) Baekryeongdo and (b) Paju from 15:00 LT to 21:00 LT on 8 August 2022. The blue box shows the backing wind pattern. (For interpretation of the references to colour in this figure legend, the reader is referred to the web version of this article.)

winds to the south of the rainfall area, is also evident in the AWSs and ocean buoys data around the area (Fig. 6). The wind data from the KHOA buoys in the northern Yellow Sea (not shown in the figure due to military security) also record northwesterly winds, confirming the contrasting wind patterns across the rainfall area. Fig. 6 shows significant variations in the wind speed across the coastline: winds much stronger over the sea (6–10 m s^{-1}; green-red scale) than the land (< 5 m s^{-1}; purple-blue scales), most likely due to the surface friction differences between the ocean and land surfaces (Zhang et al., 2019a, 2019b). In addition to the speed convergence, directional convergence is also observed over the Incheon region, characterized by the confluent flow between cyclonic flow from the low-pressure system to the north and anticyclonic flow from the high-pressure system to the south of the rain bands. These cross-coastline variations in both the wind speed and direction generate local low-level convergence and intensify temperature gradients in the coastal area west of Seoul, potentially triggering convection in conjunction with the convergence of the two air masses. Note that new convective cells continuously form at the same location in the region.

The findings above suggest that the convections are mainly triggered by the changes in the wind direction observed at Baekryeongdo, which subsequently leads to the development of a mesoscale surface front in the coastal region west of Seoul. To further investigate the factors under the upper-level wind direction change, we analyze the water vapor channel (the 6.9-μm band) from the GK-2A satellite, which provides information about the mid-level water vapor distribution (Fig. 7). In these images, wetter (drier) regions are whiter (darker). An important feature in these images is the weak dry zone (red dashed circle) over the Yellow sea, which gradually shifts southeastward over time. This zone becomes progressively darker and narrower (compare Fig. 7b and Fig. 7c). The shrinkage of this mid-level dry zone suggests the dry air is descending. Although the descending dry air may not have reached the surface, it can induce significant changes in the lower-level circulation and atmospheric instability. Park and Park (2020) showed that the interaction between the mid-level cold and dry air (400–700 hPa) and the low-level warm and humid air (700–850 hPa) during the pre-storm phase enhances atmospheric instability. Based on these analyses, we suggest that this descending dry air could contribute to the formation of the MCS by enhancing atmospheric instability. This is supported by two pieces of evidence: first, numerous convection cells are observed along the boundary of the dry zone, for instance, in inland China (not shown); second, the timing of this descending dry air coincides with the observed shifts in the low-level winds at Baekryeongdo (Fig. 5a). However, the specific role of descending small-scale cold and dry air into the large CAPE region in triggering convection has not been quantitatively addressed in observational or modeling studies. This remains a topic of future research.

4.2. Evolution of microphysical structures

This section analyzes the evolution of the distributions of hydrometeors and the raindrop size from the formation to the maturity of the convective clouds in the MCS, as they are closely related to the microphysical structure of clouds, and ultimately, rainfall intensity (Dawson et al., 2015; Sullivan et al., 2016; Mulholland et al., 2024). Fig. 8 shows CFADs (shading) and the median profiles for Z_H and Z_{DR} (solid line) in the convective region from S1 to S3 stage. In the early phase (S1), the Z_H distribution within the warm layer (below 5 km; temperatures >0 °C) is concentrated in the 35–40 dBZ range (Fig. 8a), while S2 and S3 show the highest frequencies in the 40–50 dBZ range (Fig. 8b and c, respectively). The increase in Z_H within the warm layer is indicative of heavier rainfall, suggesting that as the MCS becomes more vigorous and mature, the size and number concentration of raindrops increase. During S2, two distinct frequency peaks are noticed: one similar to that of S1 (35–40 dBZ), and another at several dBZ higher values. This bimodal distribution during S2 indicates the presence of moderate as well as particularly intense convective cells, suggesting significant rainfall during this phase.

A comparison of Z_{DR} CFADs in the warm layer shows no significant variation between the stages in the median profiles (Figs. 8d–8f). Typically, the Z_{DR} of raindrops varies with the particle shape, with larger raindrops becoming more flattened and thereby increasing in Z_{DR} (Kumjian, 2013). Thus, the increase in Z_H and the stability in Z_{DR} during MCS development suggests that the rainfall amount increase is primarily related to the rapid increase in the raindrop number concentration. Additionally, during S2 and S3, the Z_{DR} CFADs displays a larger spectrum, implying that larger raindrops are generated compared to S1.

In the cold layer (above 5 km, temperatures <0 °C), the Z_H and Z_{DR} distributions are closely related to the density and shape of snow and ice particles. Z_H tends to increase in frequency at higher levels as the MCS develops, similar to the pattern observed in the warm layer (Figs. 8a–8c). This increase indicates enhancements in the size and concentration of snow aggregates and ice particles within the cloud. The active ice-phase process is also evident in the Z_{DR} vertical profiles in the

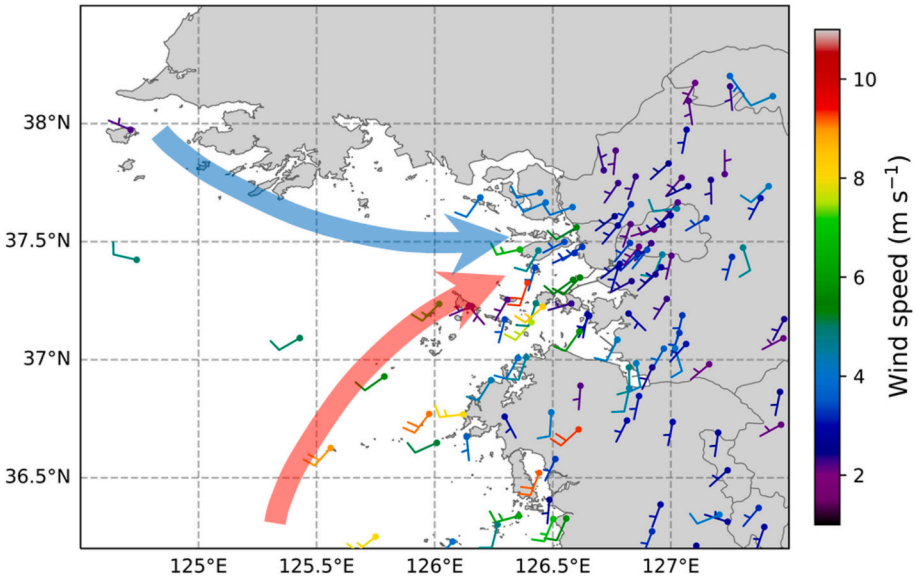


Fig. 6. Wind barbs (> 1 m s^{-1}) measured by AWS stations and ocean buoys from KMA, and by ocean research stations and tide stations from KHOA at 19:00 LT on 8 August 2022. The colors of the wind barbs indicate wind speed.

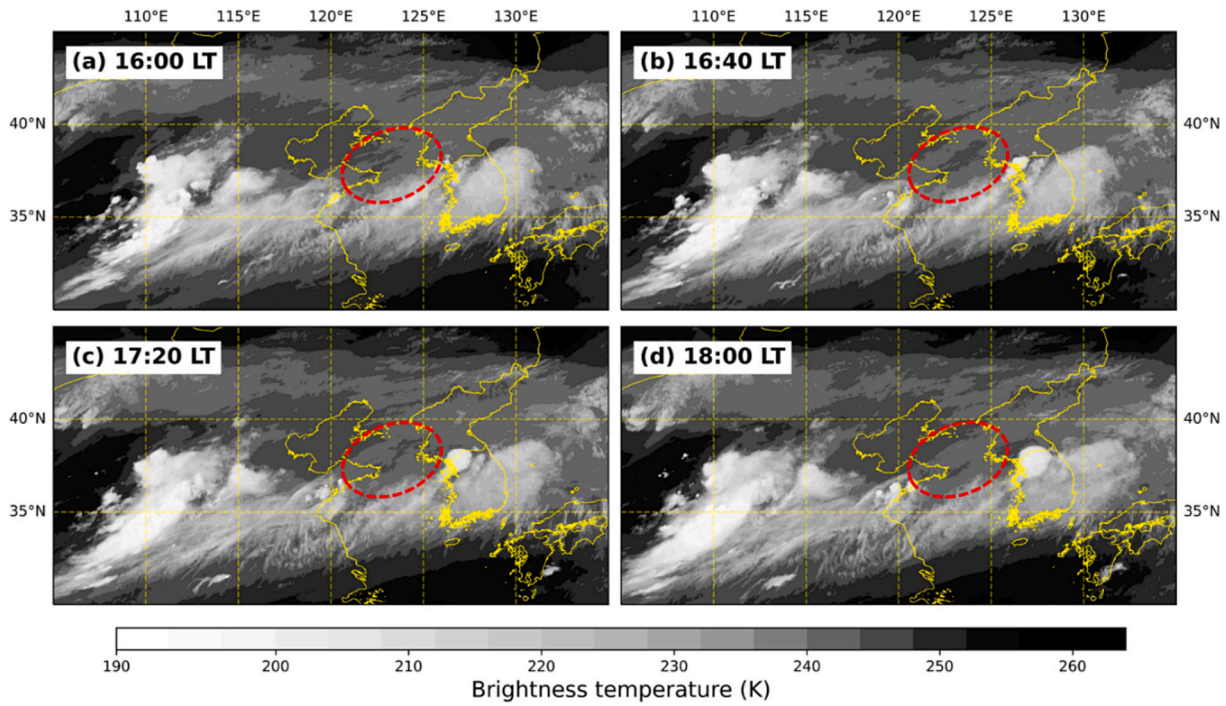


Fig. 7. Brightness temperature maps of the 6.9-μm band of the Geo-KOMAPSAT-2A (GK-2A) satellite at 40-min intervals from (a) 16:00 LT to (d) 18:00 LT on 8 August 2022.

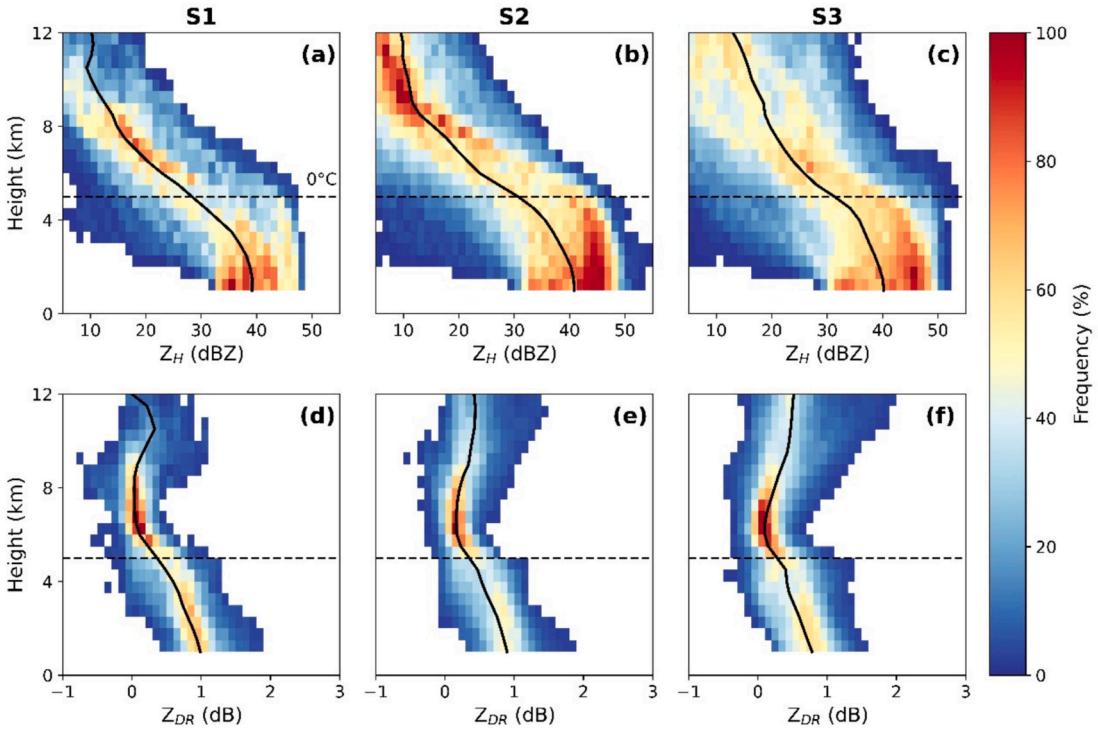


Fig. 8. Contoured frequency by altitude diagrams (CFADs) of (a) – (c) radar reflectivity (Z_H, dBZ), (d) – (f) differential reflectivity (Z_{DR}, dB) during the developmental stages of the MCS. Solid and dotted lines indicate the median profiles and 0 °C level, respectively.

cold layer. Considering that Z_{DR} changes with particle shape, the downward decrease in Z_{DR} observed in the cold layer suggests that snow and ice particles are growing to become more spherical in shape. These figures also show that the slope of Z_{DR} in the cold layer becomes progressively steeper as the MCS matures.

The CFADs for Z_H and Z_{DR} in the cold layer are linked to the variations in hydrometeors as the characteristics of radar variables change according to the size, shape, and number concentration of particles (Park et al., 2009; Kumjian, 2013; Mahale et al., 2014). The vertical distribution of hydrometeor species in each developmental stage is represented by the occurrence fractions at different altitudes in Fig. 9. This statistical analysis reduces uncertainties associated with the HCA

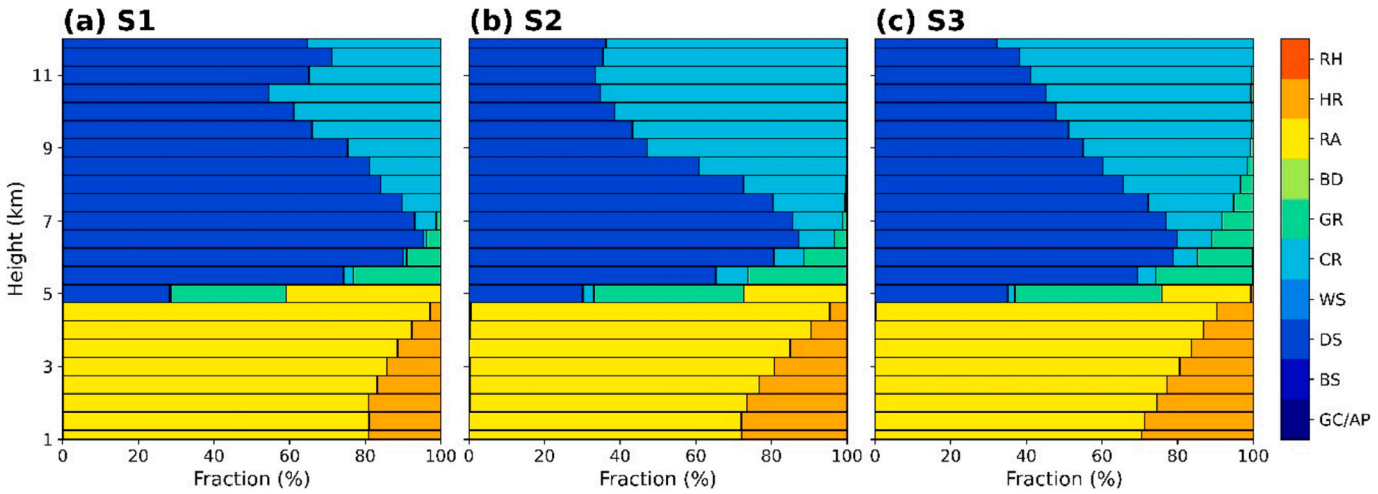


Fig. 9. Vertical distributions of occurrence fractions for different hydrometeor species during the developmental stages of this MCS.

products and identifies the dominant hydrometeor species within a specific vertical layer. Among various hydrometeors, graupel (GR, light green) is the most prominent species. As the MCS evolves, the graupel fraction gradually increases not only at the equivalent altitude, but also in higher altitudes. Because graupels are formed through the riming process (Houze Jr., 2014), the presence and growth of graupels indicate the occurrence of active riming where liquid droplets are captured by ice crystals and freeze in strong updrafts, a condition favorable for the formation of large raindrops and heavy rainfall. In addition, as the stage progresses, the fraction of not only graupel but also heavy rain (HR, shown in orange) increases below the freezing level (~5 km). This result is consistent with previous studies (Li et al., 2020; Chen et al., 2022) suggesting that the melting of graupels increases both the size and concentration of raindrops.

Shifts in the hydrometeor distribution, especially in graupel, are directly related to the vertical profile of the raindrop size and number concentrations through collision, coalescence, and breakup (Leary and Houze, 1979; Barthazy et al., 1998; Takahashi, 2006), which in turn affect rainfall intensity and type. To understand the vertical variations of the hydrometeors related to rainfall, we analyze the vertical variations of D_m, N_T, and W using CFADs and median profiles. Figs. 10a–c show that raindrops with diameters of 1.5–2 mm dominate across all three stages of MCS developments. However, the vertical distribution of raindrops larger than 2 mm evolves as the MCS matures. During the transition from S1 to S2 stage, the occurrence of larger drops increases downwards in the 1–3 km AGL, with some raindrops reaching diameters of up to ~4 mm. Simultaneously, N_T exhibits a downward decrease (Figs. 10d–f), indicating a reduction in the number concentration of raindrops. This downward decrease in raindrop numbers, combined with the increase in the raindrop size, suggests growth through collision-coalescence processes during the early stage. However, during the transition from S2 to S3, the growth of D_m stops at lower altitudes while larger raindrops (2.3–2.5 mm) begin to appear at higher altitudes (3–4 km AGL). This change can be attributed to the MCS reaching its mature

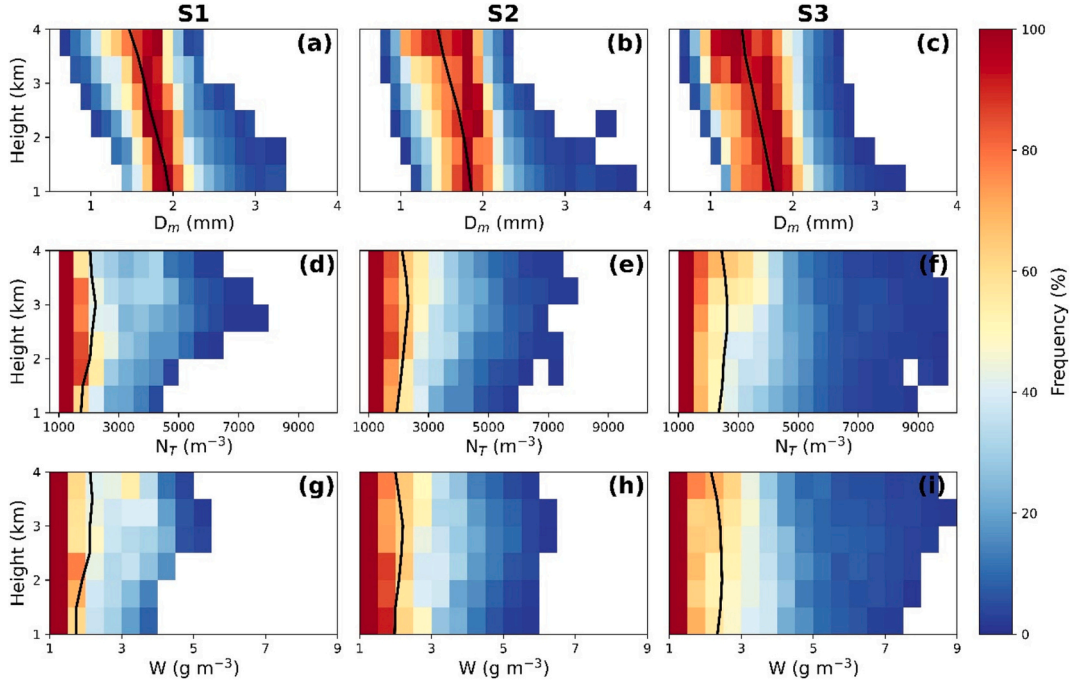


Fig. 10. CFADs of (a)–(c) mass-weighted average diameter (D_m in mm), (d)–(f) total number concentration (N_T in m^{-3}), and (g)–(i) liquid water content (W in g m^{-3}) for each stage. The black solid lines represent the median profiles.

stage, characterized by strong updrafts and an expanding downstream area that promotes more active raindrop breakup (Fovell and Tan, 1998). In S3, increased raindrop breakup leads to higher N_T values at lower altitudes, resulting in a less pronounced vertical decrease in N_T, unlike the clear downward decreasing trend observed in S1 and S2.

Figs. 10g–i display the vertical profile of the frequency of the liquid water content (W) values at different MCS development stages. As the MCS matures and surface rainfall intensifies, the W value generally increases, consistent with previous findings (e.g., Hagen and Yuter, 2003). The observed increase in W is determined primarily by the distribution of precipitating hydrometeor size and number concentration and is closely related to the increase in rainfall. Note that the W value reflects the rainwater content as cloud droplets are not detected by radar and are excluded from the W measurement. In particular, the W distribution in Fig. 10 closely resembles the N_T distribution. As the MCS matures, these CFADs further demonstrate this similarity through parallel increases in both the median and the maximum value. Furthermore, within the 1–3 km AGL layer, while D_m generally increases with decreasing height, N_T shows a decreasing pattern. During S2, the increasing pattern of D_m becomes less pronounced in the 1–1.5 km AGL layer. These contrasting vertical patterns between N_T and D_m, together with the strong similarity between W and N_T distributions, suggest that the variations in rainfall intensity are more strongly controlled by changes in N_T than those in D_m in this rainfall event.

5. Conclusion

This study analyzes observational data from multiple platforms to investigate the formation and evolution of the MCS responsible for the record-breaking rainfall in Seoul on 8 August 2022. Radar echo images show that successive convective cells form along the coastline and move eastward inland, rapidly intensifying and merging to form a zonal band-shaped MCS. Cell formations occur under atmospheric conditions characterized by synoptic-scale low-level convergence and upper-level divergences over the Korean Peninsula. Surface observations and wind profiler data show that the low-level wind direction changes from westerly to northerly at the Baekryeongdo station (northwest of the rainfall area) while southeasterly winds prevail to the south of the rainfall area. This pattern leads to the development of low-level convergence over the coastal area west of Seoul which facilitates the formation of a mesoscale surface front as two masses with different temperatures interact. Small disturbances around this front initiate convection cells, supported by the low LCL and LFC combined with a high EL, all of which indicate large CAPE. In the synoptic-scale convergence fields, the difference in the friction between the land and ocean surfaces further enhances the development of the convective cells. In addition, GK-2A satellite data shows that the low-level wind change at Baekryeongdo could be caused by the descent of dry air from the mid-level to work as another convective trigger.

The convection cells move eastward over the land by intense westerly steering-level winds to merge into a line-shaped MCS. Radar data show significant variations in the microphysical structures following the evolution of the MCS. The growth of snow and ice particles within the convective clouds becomes more pronounced, leading to overall increases in reflectivity and decreases in differential reflectivity towards lower altitudes. In particular, the growth of graupels above the melting layer (~5 km) indicates the presence of strong updrafts to increase the size and the number concentration of raindrops. Analysis of the raindrop size distribution confirms that both the size and number concentration of raindrops increase in the warm layer below 3 km AGL as the MCS develops, with the changes in number concentration being more closely related to the increase in the rainfall amount than the change in drop sizes.

This study presents the formation mechanisms and microphysical characteristics of an MCS bringing severe weather on the basis of observational data from multiple platforms. Given the large and increasing impact of localized extreme rainfall in Korea (Kim and Kim, 2020; Ho et al., 2025), our analysis and findings are expected to enhance knowledge of the meteorological factors involved in heavy mesoscale rainfall events and to contribute to the advancement of timely forecasting of such events. However, analyses of detailed structures and processes in this study are limited by the lack of fine-scale observational data. Hence, a denser observational network that can resolve the mesoscale structures of both the dynamical and thermodynamic factors is needed for a more comprehensive analysis of severe weather. Additional extreme MCS rainfall events need to be analyzed in order to understand processes and environments that can cause heavy rainfall events in Korea.

CRediT authorship contribution statement

Hee-Ae Kim: Writing – review & editing, Writing – original draft, Visualization, Validation, Methodology, Investigation, Formal analysis, Conceptualization. **Chang-Hoi Ho:** Writing – review & editing, Writing – original draft, Supervision, Funding acquisition, Conceptualization. **Jinwon Kim:** Writing – review & editing, Writing – original draft, Supervision. **Eun-Kyoung Seo:** Writing – review & editing, Validation, Formal analysis. **Seon Ki Park:** Writing – review & editing, Validation, Formal analysis.

Declaration of competing interest

The authors declare that they have no known competing financial interests or personal relationships that could have appeared to influence the work reported in this paper.

Acknowledgements

This study was funded by the Korea Meteorological Administration Research and Development Program under Grant RS-2023-00236880.

Data availability

The authors do not have permission to share data.

References

Barthazy, E., Henrich, W., Waldvogel, A., 1998. Size distribution of hydrometeors through the melting layer. Atmos. Res. 47, 193–208. https://doi.org/10.1016/S0169-8095(98)00065-9.

Biggerstaff, M.I., Houze Jr., R.A., 1991. Kinematic and precipitation structure of the 10-11 June 1985 squall line. Mon. Weather Rev. 119, 3034–3065. https://doi.org/10.1175/1520-0493(1991)119<3034:KAPSOT>2.0.CO;2.

Biggerstaff, M.I., Houze Jr., R.A., 1993. Kinematics and microphysics of the transition zone of the 10-11 June 1985 squall line. J. Atmos. Sci. 50, 3091–3110. https://doi.org/10.1175/1520-0469(1993)050<3091:KAMOTT>2.0.CO;2.

Bluestein, H.B., Jain, M.H., 1985. Formation of mesoscale lines of precipitation: Severe squall lines in Oklahoma during the spring. J. Atmos. Sci. 42, 1711–1732. https://doi.org/10.1175/1520-0469(1985)042<1711:FOMLOP>2.0.CO;2.

Brandes, E.A., Zhang, G., Vivekanandan, J., 2004a. Comparison of polarimetric radar drop size distribution retrieval algorithms. J. Atmos. Ocean. Technol. 21, 584–598. https://doi.org/10.1175/1520-0426(2004)021<0584:COPRDS>2.0.CO;2.

Brandes, E.A., Zhang, G., Vivekanandan, J., 2004b. Drop size distribution retrieval with polarimetric radar: Model and application. J. Appl. Meteorol. Climatol. 43, 461–475. https://doi.org/10.1175/1520-0450(2004)043<0461:DSDRWP>2.0.CO;2.

Chen, G., Zhao, K., Lu, Y., et al., 2022. Variability of microphysical characteristics in the "21· 7" Henan extremely heavy rainfall event. Sci. China Earth Sci. 65, 1861–1878. https://doi.org/10.1007/s11430-022-9972-9.

Cifelli, R., Petersen, W.A., Carey, L.D., Rutledge, S.A., da Silva Dias, M.A., 2002. Radar observations of the kinematic, microphysical, and precipitation characteristics of two MCSs in TRMM LBA. J. Geophys. Res. Atmos. 107. https://doi.org/10.1029/2000JD000264. LBA–44.

Corfidi, S.F., 2003. Cold pools and MCS propagation: forecasting the motion of downwind-developing MCSs. Weather Forecast. 18, 997–1017. https://doi.org/10.1175/1520-0434(2003)018<0997:CPAMPF>2.0.CO;2.

Craven, J.P., Jewell, R.E., Brooks, H.E., 2002. Comparison between observed convective cloud-base heights and lifting condensation level for two different lifted parcels. Weather Forecast. 17, 885–890. https://doi.org/10.1175/1520-0434(2002)017<0885:CBOCCB>2.0.CO;2.

Davis, C., Atkins, N., Bartels, D., et al., 2004. The bow echo and MCV experiment: Observations and opportunities. Bull. Am. Meteorol. Soc. 85, 1075–1094. https://doi.org/10.1175/BAMS-85-8-1075.

Dawson, D.T., Mansell, E.R., Kumjian, M.R., 2015. Does wind shear cause hydrometeor size sorting? J. Atmos. Sci. 72, 340–348. https://doi.org/10.1175/JAS-D-14-0084.1.

Feng, Z., Leung, L.R., Liu, N., et al., 2021. A global high-resolution mesoscale convective system database using satellite-derived cloud tops, surface precipitation, and tracking. J. Geophys. Res. Atmos. 126, e2020JD034202. https://doi.org/10.1029/2020JD034202.

Fovell, R.G., Tan, P.H., 1998. The temporal behavior of numerically simulated multicell-type storms. Part II: the convective cell life cycle and cell regeneration. Mon. Weather Rev. 126, 551–577. https://doi.org/10.1175/1520-0493(1998)126<0551:TTBONS>2.0.CO;2.

Hagen, M., Yuter, S.E., 2003. Relations between radar reflectivity, liquid-water content, and rainfall rate during the MAP SOP. Q. J. R. Meteorol. Soc. 129, 477–493. https://doi.org/10.1256/qj.02.23.

Ho, C.-H., Kim, -H.-A., Cha, Y., Do, H.-S., Kim, J., Kim, J., Park, S.K., Yoo, H.-D., 2025. Recent changes in summer rainfall characteristics in Korea. J. Europ. Meteorol. Soc. 2, 100009. https://doi.org/10.1016/j.jemets.2025.100009.

Ho, J., Zhang, G., Bukovcic, P., Parsons, D.B., Xu, F., Gao, J., Carlin, J.T., Snyder, J.C., 2023. Improving polarimetric radar-based drop size distribution retrieval and rain estimation using a deep neural network. J. Hydrometeorol. 24, 2057–2073. https://doi.org/10.1175/JHM-D-22-0166.1.

Holton, J.R., 2004. An Introduction to Dynamic Meteorology, fourth ed. Academic press, San Diego.

Houze Jr., R.A., 2014. Cloud Dynamics, second ed. Academic Press, San Diego.

Houze Jr., R.A., Rutledge, S.A., Biggerstaff, M.I., Smull, B.F., 1989. Interpretation of Doppler weather radar displays of midlatitude mesoscale convective systems. Bull. Amer. Meteor. Soc. 70, 608–619. https://doi.org/10.1175/1520-0477(1989)070<0608:IODWRD>2.0.CO;2.

Houze Jr., R.A., Smull, B.F., Dodge, P., 1990. Mesoscale organization of springtime rainstorms in Oklahoma. Mon. Weather Rev. 118, 613–654. https://doi.org/10.1175/1520-0493(1990)118<0613:MOOSRI>2.0.CO;2.

Hu, H., Leung, L.R., Feng, Z., 2020. Observed warm-season characteristics of MCS and non-MCS rainfall and their recent changes in the Central United States. Geophys. Res. Lett. 47, e2019GL086783. https://doi.org/10.1029/2019GL086783.

Jeong, J.-H., Lee, D.-I., Wang, C.-C., Han, I.-S., 2016. Characteristics of mesoscale-convective-system-produced extreme rainfall over southeastern South Korea: 7 July 2009. Nat. Hazards Earth Syst. Sci. 16, 927–939. https://doi.org/10.5194/nhess-16-927-2016.

Jirak, I.L., Cotton, W.R., 2007. Observational analysis of the predictability of mesoscale convective systems. Weather Forecast. 22, 813–838. https://doi.org/10.1175/WAF1012.1.

Johnson, R.H., Hamilton, P.J., 1988. The relationship of surface pressure features to the precipitation and airflow structure of an intense midlatitude squall line. Mon. Weather Rev. 116, 1444–1473. https://doi.org/10.1175/1520-0493(1988)116<1444:TROSPF>2.0.CO;2.

Kim, K.-Y., Kim, B.-S., 2020. The effect of regional warming on the East Asian summer monsoon. Clim. Dyn. 54, 3259–3277. https://doi.org/10.1007/s00382-020-05169-7.

Kim, H.W., Lee, D.K., 2006. An observational study of mesoscale convective systems with heavy rainfall over the Korean Peninsula. Weather Forecast. 21, 125–148. https://doi.org/10.1175/WAF912.1.

Kim, D., Gu, M., Oh, T.-H., Kim, E.-K., Yang, H.-J., 2021. Introduction of the advanced meteorological imager of Geo-Kompsat-2a: In-orbit tests and performance validation. Remote Sens. 13, 1303. https://doi.org/10.3390/rs13071303.

Kim, H.-A., Ho, J., Zhang, G., Ha, K.-J., Hong, S.-Y., Ho, C.-H., 2024. Polarimetric radar signatures in various lightning activities during Seoul (Korea) flood on August 8, 2022. Asia-Pac J. Atmospheric Sci 60, 1–15. https://doi.org/10.1007/s13143-023-00346-0.

Korea Meorological Administration (KMA), 2023. Practical Guide to Forecasting Techniques: User Manual for Thermodynamic Diagrams. KMA. https://www.kma.go.kr/down/e-learning/hands/hands_09.pdf (in Korean).

Kumjian, M.R., 2013. Principles and applications of dual-polarization weather radar. Part I: Description of the polarimetric radar variables. J. Oper. Meteorol. 1, 226–242. https://doi.org/10.15191/nwajom.2013.0119.

Leary, C.A., Houze, R.A., 1979. Melting and evaporation of hydrometeors in precipitation from the anvil clouds of deep tropical convection. J. Atmos. Sci. 36, 669–679. https://doi.org/10.1175/1520-0469(1979)036<0669:MAEOHI>2.0.CO;2.

Lee, T.-Y., Kim, Y.-H., 2007. Heavy precipitation systems over the Korean peninsula and their classification. Asia-Pac J Atmospher. Sci. 43, 367–396.

Lee, J., Jin, H.-G., Baik, J.-J., 2023. Diagnostic relations for the intercept parameter of exponential raindrop size distribution according to rain types derived from disdrometer data and their impacts on precipitation prediction. Asia-Pac J. Atmospheric Sci 59, 219–238. https://doi.org/10.1007/s13143-022-00306-0.

Li, H., Wan, Q., Peng, D., Liu, X., Xiao, H., 2020. Multiscale analysis of a record-breaking heavy rainfall event in Guangdong, China. Atmos. Res. 232, 104703. https://doi.org/10.1029/2000JD000264.

Maddox, R.A., 1980. Mesoscale convective complexes. Bull. Amer. Meteor. Soc. 61, 1374–1387. https://doi.org/10.1175/1520-0477(1980)061<1374:MCC>2.0.CO;2.

Mahale, V.N., Zhang, G., Xue, M., 2014. Fuzzy logic classification of S-band polarimetric radar echoes to identify three-body scattering and improve data quality. J. Appl. Meteorol. Climatol. 53, 2017–2033. https://doi.org/10.1175/JAMC-D-13-0358.1.

Mulholland, J.P., Nowotarski, C.J., Peters, J.M., Morrison, H., Nielsen, E.R., 2024. How does vertical wind shear influence updraft characteristics and hydrometeor distributions in supercell thunderstorms? Mon. Weather Rev. 152, 1663–1687. https://doi.org/10.1175/MWR-D-23-0166.1.

Park, S.K., Park, S., 2020. On a flood-producing coastal mesoscale convective storm associated with the Kor'easterlies: Multi-data analyses using remotely-sensed and in-situ observations and storm-scale model simulations. Remote Sens. 12, 1532. https://doi.org/10.3390/rs12091532.

Park, H.S., Ryzhkov, A.V., Zrnić, D.S., Kim, K.-E., 2009. The hydrometeor classification algorithm for the polarimetric WSR-88D: Description and application to an MCS. Weather Forecast. 24, 730–748. https://doi.org/10.1175/2008WAF2222205.1.

Parker, M.D., Johnson, R.H., 2000. Organizational modes of midlatitude mesoscale convective systems. Mon. Weather Rev. 128, 3413–3436. https://doi.org/10.1175/1520-0493(2001)129<3413:OMOMMC>2.0.CO;2.

Peters, J.M., Nielsen, E.R., Parker, M.D., Hitchcock, S.M., Schumacher, R.S., 2017. The impact of low-level moisture errors on model forecasts of an MCS observed during PECAN. Mon. Weather Rev. 145, 3599–3624. https://doi.org/10.1175/MWR-D-16-0296.1.

Rasmussen, K.L., Zuluaga, M.D., Houze Jr., R.A., 2014. Severe convection and lightning in subtropical South America. Geophys. Res. Lett. 41, 7359–7366. https://doi.org/10.1002/2014GL061767.

Rasmussen, K.L., Chaplin, M.M., Zuluaga, M.D., Houze Jr., R.A., 2016. Contribution of extreme convective storms to rainfall in South America. J. Hydrometeorol. 17, 353–367. https://doi.org/10.1175/JHM-D-15-0067.1.

Rowe, A.K., Houze Jr., R.A., 2014. Microphysical characteristics of MJO convection over the Indian Ocean during DYNAMO. J. Geophys. Res. Atmos. 119, 2543–2554. https://doi.org/10.1002/2013JD020799.

Schumacher, R.S., 2017. Heavy Rainfall and Flash Flooding. Encycl. of Nat. Hazard Sci, Oxford Res. https://doi.org/10.1093/acrefore/9780199389407.013.132.

Schumacher, R.S., Johnson, R.H., 2005. Organization and environmental properties of extreme-rain-producing mesoscale convective systems. Mon. Weather Rev. 133, 961–976. https://doi.org/10.1175/MWR2899.1.

Steiner, M., Houze Jr., R.A., Yuter, S.E., 1995. Climatological characterization of three-dimensional storm structure from operational radar and rain gauge data. J. Appl. Meteorol. Climatol. 34, 1978–2007. https://doi.org/10.1175/1520-0450(1995)034<1978:CCOTDS>2.0.CO;2.

Sullivan, S.C., Lee, D., Oreopoulos, L., Nenes, A., 2016. Role of updraft velocity in temporal variability of global cloud hydrometeor number. Proc. Natl. Acad. Sci. 113, 5791–5796. https://doi.org/10.1073/pnas.1514039113.

Takahashi, T., 2006. Precipitation mechanisms in east Asian monsoon: Videosonde study. J. Geophys. Res. Atmos. 111, D09202. https://doi.org/10.1029/2005JD006268.

Wandishin, M.S., Stensrud, D.J., Mullen, S.L., Wicker, L.J., 2008. On the predictability of mesoscale convective systems: Two-dimensional simulations. Weather Forecast. 23, 773–785. https://doi.org/10.1175/2008WAF2007057.1.

Wandishin, M.S., Stensrud, D.J., Mullen, S.L., Wicker, L.J., 2010. On the predictability of mesoscale convective systems: Three-dimensional simulations. Mon. Weather Rev. 138, 863–885. https://doi.org/10.1175/2009MWR2961.1.

Wang, H., Luo, Y., Jou, B.J.D., 2014. Initiation, maintenance, and properties of convection in an extreme rainfall event during SCMREX: Observational analysis. J. Geophys. Res. Atmos. 119, 13–206. https://doi.org/10.1002/2014JD022339.

Wilde, N.P., Stull, R.B., Eloranta, E.W., 1985. The LCL zone and cumulus onset. J. Appl. Meteorol. Climatol. 24, 640–657. https://doi.org/10.1175/1520-0450(1985)024<0640:TLZACO>2.0.CO;2.

Wu, M., Luo, Y., 2016. Mesoscale observational analysis of lifting mechanism of a warm-sector convective system producing the maximal daily precipitation in China mainland during pre-summer rainy season of 2015. J. Meteorol. Res. 30, 719–736. https://doi.org/10.1007/s13351-016-6089-8.

Xu, W., Zipser, E.J., Chen, Y.-L., Liu, C., Liou, Y.C., Lee, W.-C., Jong-Dao Jou, B., 2012. An orography-associated extreme rainfall event during TiMREX: Initiation, storm evolution, and maintenance. Mon. Weather Rev. 140, 2555–2574. https://doi.org/10.1175/MWR-D-11-00208.1.

Yin, J., Albertson, J.D., Rigby, J.R., Porporato, A., 2015. Land and atmospheric controls on initiation and intensity of moist convection: CAPE dynamics and LCL crossings. Water Resour. Res. 51, 8476–8493. https://doi.org/10.1002/2015WR017286.

Yuter, S.E., Houze Jr., R.A., 1995. Three-dimensional kinematic and microphysical evolution of Florida cumulonimbus. Part II: Frequency distributions of vertical velocity, reflectivity, and differential reflectivity. Mon. Weather Rev. 123, 1941–1963. https://doi.org/10.1175/1520-0493(1995)123<1941:TDKAME>2.0.CO;2.

Zhang, L., Min, J., Zhuang, X., Schumacher, R.S., 2019a. General features of extreme rainfall events produced by MCSs over East China during 2016–17. Mon. Weather Rev. 147, 2693–2714. https://doi.org/10.1175/MWR-D-18-0455.1.

Zhang, Z., Wang, K., Chen, D., Li, J., Dickinson, R., 2019b. Increase in surface friction dominates the observed surface wind speed decline during 1973–2014 in the Northern Hemisphere lands. J. Clim. 32, 7421–7435. https://doi.org/10.1175/JCLI-D-18-0691.1.

Zipser, E.J., 1977. Mesoscale and convective-scale downdrafts as distinct components of squall-line structure. Mon. Weather Rev. 105, 1568–1589. https://doi.org/10.1175/1520-0493(1977)105<1568:MACDAD>2.0.CO;2.